Investigation of Local Hydrogen Uptake in Rescaled Model Occluded Sites using Crevice Scaling Laws

John R. Scully and Michael Switzer

Investigation of Local Hydrogen Uptake in Rescaled Model Occluded Sites using Crevice Scaling Laws

John R. Scully, Michael A. Switzer

Center for Electrochemical Science and Engineering

Department of Materials Science and Engineering,

The University of Virginia

Charlottesville, VA 22904, USA

Abstract

The effects of occluded site geometry and applied potential on hydrogen production and uptake in a martensitic stainless steel (Fe-13Cr-8Ni-2Mo-1Al) were explored. On planar electrode surfaces, the total hydrogen concentration was found to increase exponentially with hydrogen overpotential. The x^2/gap scaling law, where x is the pit/crevice depth and "gap" is the pit/crevice width, was utilized to rescale model pits from micrometer to millimeter dimensions. Such rescaling enabled local hydrogen measurements as a function of pit depth in rescaled pits. Two values of x_{crit} were identified. Significant local hydrogen (H) uptake was observed at $x > x_{crit}$ under conditions where external surfaces were in a passive state and above the hydrogen electrode potential ($E_{H/H+}$). The local potential drops below $E_{H/H+}$ at a depth, $x_{crit1} = x_{HER}$ and reaches the primary passivation potential (E_{Pass}) of the stainless steel at a depth, $x_{crit2} = x_{Pass}$. Thus, at $x > x_{crit1}$, the stainless steel experiences H production and uptake but remains passivated. At $x > x_{crit2}$, the material absorbs hydrogen on an actively dissolving pit surfaces since the local potential drops below E_{Pass}. Nuclear reaction analysis revealed that concurrent metal dissolution

20060710053

and hydrogen uptake lead to significant amounts of local hydrogen absorption just beneath simulated pit surfaces.

1. INTRODUCTION

Pits and other occluded sites serve several roles that promote stress corrosion cracking and hydrogen environment-assisted cracking (HEAC) of engineering alloys in aqueous environments.[1,2,3] Pits can act as stress concentrators that facilitate crack initiation, expose susceptible grain boundaries and interfaces not available on machined surfaces, and provide an occluded site enabling locally aggressive environment formation. For instance, the acidic environment of freely corroding and anodically polarized pits or crevices with actively corroding surfaces can promote accelerated corrosion as well as H production and entry. The latter occurs as a consequence of hydrolytic acidification of dissolved metal cations and ohmic potential drop such that the pit bottom potential is near or below the reversible hydrogen electrode potential, $E_{H/H+}$. Hydrolysis of metal cations can drastically lower the pH of the occluded site such as a pit or crack so that it is much more acidic than the bulk solution.[4] This may enhance the proton reduction reaction depending on reaction order with respect to proton activity and also affect the exchange current density for proton reduction. Moreover, acidification may lead to depassivation and activation of the occluded site surfaces by chemical dissolution of any pre-existing oxide film that limits H production and uptake. In addition, ohmic potential drop, as a function of the pit geometry and the solution resistance of the pit electrolyte, may promote activation of a passive metal when the local potential falls below the Flade potential or the primary passive potential, E_{Pass}, even though the external surface of the metal is held at a potential where it is passive. Moreover, the local potential may drop below $E_{H/H+}$ enabling generation of H that can readily diffuse into the metal. Furthermore, metal oxidation or selective dissolution of on element in a solid solution alloy can inject vacancies into the metal [5] that forms clusters, [6] alter other aspects its near-surface metallurgical condition such as changing the near surface composition or causing void formation [7] as well as possibly triggering dynamic trap state

creation when vacancies function as H traps. [8] The amount of H generation within the pit coupled with slow effective H diffusivity within a trap-rich high-strength steel could result in large local H concentrations at such pits or crevices sites, despite the large chemical driving force for H diffusion into the metal. These factors may lead to an underestimation of subsurface diffusible and trapped H concentrations in H uptake experiments that sample global H concentrations averaged over large areas and volumes.

A critical unresolved issue in HEAC is the local crack tip H concentration. This information may not be accessible by conventional analysis and may differ from global hydrogen concentrations over large sampling area as discussed above. Quantifying H uptake and local H concentrations in pits, crevices and cracks is difficult due to the size scale of the damage process zone particular at environmental crack tips where crack surface opening displacements underestimate continuum predictions.[9] The solution chemistry within HEAC sites has been determined by freezing and isolating the solution present in the crack tip, and using indicator papers to identify the solution pH and the presence of metal ions.[10] Recently, capillary electrophoresis has been used.[11] While these procedures determine the presence of certain ions within the crack tip solution, few methods for measuring local H concentrations have been employed. A crevice chamber has been added to the charging side of a Devanthan permeation cell in order to simulate an occluded site.[12,13] However, precise crevice scaling in order to duplicate the electrochemical conditions of a smaller sized crack or pit was not considered. Secondary ion mass spectroscopy and tritium detection methods show large increases in hydrogen concentrations near actual crack tips but often lack spatial resolution to probe sharp crack tips.[14,15] Experiments utilizing thermal emission methods for determining total H concentrations require a large sample mass. Therefore, such techniques generally yield globally averaged concentrations, which cannot capture the presence of severe H concentration gradients such as might exists at the tip of a crack or in a pit. Large scale H permeation measurements using a charging solution that mimics the composition of acid pits may not reproduce the exact chemistry, surface state, metallurgy or electrochemistry of the metal within occluded sites. Furthermore, high pit dissolution rates may alter the near surface metallurgy of pits and thickness changes during permeation confound accurate measurements. Micron-scale potential changes and chemical gradients in real pits, crevices and cracks are difficult to quantify and reproduce with large commercial microelectrodes given the micro-liter solution volumes present at real

occluded sites. The bulk solutions used in permeation experiments are approximations of the solutions in real pits. Consequently, it is difficult to accurately quantify H uptake in pits. It is possible that poorly understood local factors at real cracks, pits and crevices conspire to produce high local H concentrations that would be absent in planar electrode experiments with simulated occluded sites chemistries. Knowledge of the relevant crack tip concentration is a critical unresolved issue in HEAC. This information is required to forecast HEAC susceptibility as a function of electrochemical conditions such as potential and possible mitigation strategies. This is especially important when the damage mechanism involves crack initiation when the local hydrogen concentration exceeds a critical concentration over a critical depth at a sharp crack tip.[16]

Precipitation-aged hardened martensitic stainless steels (i.e., Fe-Cr-Ni-Mo alloys) that release hydrolysable Cr and Fe cations during electrodissolution are ideal candidates for intensified local H uptake at anodically polarized pits, crevices or cracks not otherwise seen in global measurements of H absorption. These alloys, at high strength levels, also have known to be susceptible to internal hydrogen embrittlement and HEAC, and are extremely sensitive to crack tip H concentration.[17] Cathodic polarization to introduce global uniform hydrogen levels show clear evidence of environmental hydrogen embrittlement.[18] Such steels are quite susceptible to acid pitting, resulting in sufficient ohmic voltage drop and local acidification to promote H production and uptake in pits and crevices.[19] Under such conditions, external surfaces remain passive and at electrochemical potentials above E_{H/H^+}, while H production and absorption occurs inside pits.[20] Slow effective diffusion rates restrict rapid transport of high levels of diffusible H away from hot spots such as pits where local H uptake may be severe[25] For instance, K_{Th} differs significantly for open-circuit potential (OCP) exposure in 3.5% NaCl versus 20% NaCl, which likely establishes a different set of electrochemical conditions such as OCP, resulting in a different local crack tip chemistry and level of H uptake.[21]. The K_{th} vs yield strength data for PH 13-8 Mo suggest an extreme sensitivity to electrochemical conditions that enable such local H uptake.

There is a need to develop a better understanding of the conditions under which pits and recesses might promote local H production and uptake when H production and uptake is not expected such as at open circuit and under anodic polarization, and to quantify local H concentrations. One approach is to exploit pit scaling laws.[20],[22] This paper characterizes local

H concentrations over small length scales in model pits in a precipitation-hardened martensitic stainless steel, utilizing appropriate geometric crevice scaling laws to design and manufacture model pits of millimeter dimensions that are analogous to actual pits of micrometer scale dimensions. These pits were then used to examine H uptake at various locations within the pits under selected electrochemical conditions. Quantification of the absorbed hydrogen was facilitated by the use of thermal desorption spectroscopy (TDS) and nuclear reaction analysis (NRA). Both have the ability to analyze small-scale samples. NRA has extremely good depth resolution with a millimeter lateral scale resolution, This paper demonstrates the concept of occluded site rescaling for the purposes of local hydrogen measurement.

2. APPROACH

2.0 Materials

The focus for investigation of local H uptake was a precipitation-hardened stainless steel, PH 13-8 Mo stainless steel, (H1050 condition, σ_{YS} = 1241 MPa, K_{IC} = 96-165 MPa$\sqrt{m}$). The alloy composition indicated in Table 1 was selected for investigation. In preliminary experiments, constant temperature TDS experiments were performed to determine the effective diffusion behavior (D_{eff}). D_{eff} was found to follow an Arrhenius text expression with an effective activation energy of 21.1 kJ/mole.

$$D_{eff}(T) = (9.25 \times 10^{-5} \text{ cm}^2/\text{sec}) \ \exp[-\frac{21.1 kJ/mole}{RT(K)}]$$
[Eq. 1]

This expression yields a diffusion coefficient at 25 °C of 1.9 x10^{-8} cm^2/sec consistent with a temper martensitic microstructure containing secondary hardening precipitates.[21] Both planar electrodes and model rescaled localized corrosion sites were studied under conditions mimicking those encountered during acid pitting.

Table 1. Composition of PH 13-8 Mo Stainless Steel

	Cr	Ni	Mo	Al	Mn	C	Si	P	S	N	Fe
Wt. %	12.5	8.14	2.12	1.1	0.09	0.03	0.04	0.006	0.0004	0.005	75.97
At. %	13.3	7.66	1.22	2.3	0.09	0.14	0.08	0.011	0.001	0.020	75.24

2.1 Hydrogen Analysis

TDS was utilized to quantify absorbed H concentrations in model-occluded sites. The TDS system utilizes a quadrupole mass spectrometer to measure the change in H_2 partial pressure via monitoring of selected mass/charge ratios in a high vacuum chamber containing a H charged sample that is the source of the outgassing.[23] H analysis was measured from specimens cut from rescaled pits less than one gram in mass and less than 0.1 cm^3. The amount of H outgassed is dependent on the programmed temperature of the furnace surrounding the analysis chamber since the total H released at a given temperature includes both diffusible and trapped H.[24] H trapping sites within PH 13-8 Mo include grain and lath boundaries, dislocations and strengthening precipitates. Each trapping site has an associated binding energy.[25] A programmed ramp rate of $3°C/min$ from room temperature to a maximum temperature of $330°C$ was confirmed to release H from lattice and major trap states. The integrated amount of hydrogen released was used to quantify the global diffusible and trap-affected hydrogen concentrations in specimens removed from LN_2 storage after potentiostatic polarization. This was conducted after subtraction of the background hydrogen level detected before hydrogen charging. Nuclear reaction analysis was performed on hydrogen charged planar electrodes of PH 13-8 Mo at the ion beam facility at the University of Albany of New York. Hydrogen was detected using $^1H(^{15}N,\gamma\alpha)^{12}C$ nuclear reaction (6.385+/- 0.005 MeV resonant energy) using a beam of high-energy $^{15}N^+$ ions to bombard a sample over a lateral area of square millimeters. The gamma ray output results from the nuclear reaction of the N^{15} ions with atomic hydrogen and is proportional to the hydrogen concentration over a finite depth range. Depth profiling is achieved by varying the kinetic energy of the ionized nitrogen beam above the threshold resonant energy. In this way the beam of N^{15} ions penetrated the material, energy loss occurred, and the resonant energy was achieved at a given sample depth. Thus the gamma ray output was proportional to hydrogen concentration at that depth. In this way, energy loss was exploited to sample hydrogen concentration over precise ranges of depth perpendicular to planar electrode surfaces. A depth resolution of a few nanometers is achieved due to the four order of magnitude difference in cross-section and hence gamma-ray yields at the resonance energy compared to off-resonance energies.

2.2 Planar Electrode Experiments to Measure Hydrogen Uptake

Studies were conducted on planar electrodes exposed to room temperature deaerated solutions of 0.1 M HCl (simulating an acidic solution associated with occluded sites) and 5 M H_2SO_4 solution (pH = -0.57) plus dissolved iron, chromium, and nickel ions (simulating a acid pit environment in a stainless steel after metal dissolution). A Hg/Hg_2SO_4/sat. K_2SO_4 reference electrode was used in H_2SO_4 (+640 mV vs. SHE at 25°C). A saturated calomel electrode was used in HCl solutions (+241 mV vs. SHE at 25°C). Cathodic E-Log(i) data were analyzed over a range of pH levels to provide reaction kinetics for the H evolution reaction (HER) as a function of pH and cathodic H overpotential. The volume of hydrogen gas generated during potentiostatic polarization was collected and determined volumetrically with an inverted funnel/burret system. H uptake was subsequently studied by TDS at selected potentials. TDS was used to characterize steady state total hydrogen concentrations, C_H, under conditions where bulk H charging occurs at cathodic potentials, under local pitting conditions, as well as under conditions promoting pit depassivation and surface activation simultaneous with H production. TDS was performed on planar electrodes charged for time periods enabling homogeneous distributions in H concentration. TDS and NRA were performed on exposed materials that were charged for time periods enabling homogeneous distributions in H concentration. Two separate cleaning procedures were used (methanol rinse and nitric acid cleaning) and specimens were immediately stored in LN_2. TDS analysis of the hydrogen charged samples was used to produce relationships between absorbed hydrogen concentration and charging potential.

2.3 Rescaling Methods to Enable Spatially Resolved H Analysis in Pits

Local corrosion scaling laws were implemented to duplicate occluded site conditions representative of a small pit or crevice in larger sized "rescaled" model pits more accessible to H measurements but able to reproduce equivalent mass transport, ohmic potential and electrochemical properties over larger scaled dimensions. The precise scaling laws that apply to PH 13-8 Mo were identified using the *CREVICERv2.0* computer program.[26] Various pit geometries were modeled using actual experimental electrochemical parameters obtained from PH 13-8 Mo such as critical current density, passive current density and E_{Pass}. The modeled pit geometry contained a square crevice opening and depth to produce a pit cavity shaped as a right angle prism. The pit mouth dimension is analogous to a crevice gap (G) and represents the edge

length of the square pit mouth The potential distribution was determined as a function of the pit depth dimension (x) for various pit mouth dimensions. Relationships between two critical depths -- the depth for depassivation and activation of the stainless steel in an acid, $x_{crit1} = x_{Pass}$, as well as the depth for the local potential to drop below the reversible H potential, $x_{crit2} = x_{HER}$ -- were developed for a given pit gap. Relationships between x_{crit}^2 vs. gap were then developed over a range of G. Complexity was reduced by conducting experiments and modeling in 5M H_2SO_4 containing metal salts that minimized pit chemistry variations as a function of pit depth so that a single electrochemical boundary condition could be utilized at all positions in the pit. After constructing plots of local potential versus depth, x, for various applied potentials at the pit mouth and dimensions G, x_{crit1} and x_{crit2} were plotted versus G.[27,28] The nearly linear x^2/G relationships obtained served as scaling laws that guided development of rescaled pits for experimental study by enabling specification and fabrication of larger dimension pits with a cylindrical occluded sites capable of allowing spatially resolved H measurements. These pits were electrochemically equivalent to small-scale versions of occluded sites with the exception that H_2 bubble, corrosion-salt film formation and dynamic straining were not incorporated. Bubbles restrict ionic transport in crevices and pits, and are expected to induce greater IR drop. However, recesses subjected to H evolution were previously found to follow the x^2/G relationship when equivalence of Tafel kinetics was considered.

Experimentally, rescaled pit specimens were potentiostatically charged under conditions where the pit mouth resided in the passive region and H uptake was possible given sufficient IR drop at a certain pit depth. Specimens were held under these conditions until uniformly charged from interior surfaces of the rescaled pit according to the H diffusivity in PH 13-8 Mo. Micro-reference electrode measurements (World Precision Instruments Driref-450 Micro-ref. Electrode) recorded local pit potential as a function of pit depth, x, using a micrometer resolution positioning system. Thus, the depth at which the local potential dropped below E_{Pass} and $E_{H/H+}$ could be determined by comparison of E-log(i) and $E_{H/H+}$ to potential distributions. C_H versus rescaled pit depth profiles were constructed by two methods. Cylindrical pits were stored in LN_2, cold sectioned at various depths from the exposed pit mouth and analyzed by TDS to measure global H concentration, C_H, in slices cut perpendicular to the x direction at various pit depths. Secondly, the previously established relationships between C_H versus IR corrected electrochemical charging potential obtained from planar electrodes were used. Local potential

distributions within pits were compared to planar electrode data at precise potentials to predict the potential dependent C_H, anodic, i_{an}, as well as cathodic, i_{ca}, half-cell reaction rates.

3. RESULTS

3.1 Electrochemistry Associated with Passive-to-Active Transitions and HER

E-Log(i) polarization data for PH 13-8 Mo exposed to various concentrations of sulfuric acid containing dissolved metal ions can be seen in Figure 1. PH 13-8 Mo exhibits an active-passive transition in each of these solutions. A passive region is seen above approximately –0.5 $V_{Hg/Hg2SO4}$. The alloy exposed to 5 M H_2SO_4 plus dissolved metal ions shows a large critical current density of approximately 3 x 10^{-3} A/cm^2. A 5M H_2SO_4 solution was chosen to examine H uptake in the model pits. The reversible H potential for this solution is -0.59 $V_{Hg/Hg2SO4}$. It is possible that a rescaled pit or crevice held in the passive range would undergo a passive-to-active transition and the OCP of the crevice could fall below –0.75 $V_{Hg/Hg2SO4}$. A the simplified version of Fig. 1 was used as the E-log(i) boundary condition in CREVICERv2 using i_{pass}, i_{crit}, and E_{pass} from 5M H_2SO_4.

Figure 2 shows the E-logi behavior for PH 13-8 Mo in deaerated 0.1M NaCl. A passive region is observed with characteristic current increases upon pitting. In 0.5 and 1 M HCl, active polarization behavior is observed. The alloy exposed to 0.1 M HCl solution exhibits a several hundred mV passive range above reversible hydrogen where minimal hydrogen production and uptake would be expected. This solution was chosen for focus of remaining experiments.

Concerning the HER deaerated sulfuric acid plus 0.1 M Fe^{+2}, 0.018 M Cr^{+3} and 0.01 M Ni^{+2} solutions at 25 °C., IR correction of the cathodic E-Log(i) data was used to generate an expression for cathodic HER current density as a function of H overpotential and pH:

$$i_{H_2} = (1.31 \times 10^{-4})[H^+]^{0.525} \exp(-14.45\eta_c)$$
[Eq. 2]

where i_{H2} is the cathodic HER current density (A/cm^2), [H$^+$] is the hydronium ion concentration (mole/L) and η_c is the H overpotential (V). The Tafel slope was ~160 mV/decade. For a given solution pH, Equation 2 can be used to predict the cathodic current density at various hydrogen overpotentials as illustrated in Figure 3.

The cathodic E-Log(i) data were IR corrected and an expression for cathodic current density as a function of pH and overpotential was also developed for 0.1 M HCl:

$$i_{H_2} = (5.45 \times 10^{-5})[H^+]^{0.185} \exp(-12.74\eta_c) \qquad \text{[Eq. 3]}$$

where i_{H2} is the HER current density (A/cm^2), [H$^+$] is the hydronium ion concentration (mole/L), and η_c is the hydrogen overpotential (V). This expression is consistent with an HER Tafel slope of 181 mV/decade. This expression, again, enables determination of hydrogen evolution half-cell reaction rates over a broad potential range including prediction of i_{H2} where the applied current density is net anodic.

3.2 Global Hydrogen Uptake on Planar Electrodes as a Function of IR-Corrected Potential

Planar samples of PH 13-8 Mo anodically and cathodically polarized in 0.1 M HCl and in 5 M sulfuric acid plus dissolved metal ions were analyzed to determine C_H, adsorbed after charging to achieve a homogeneous global H distribution considering the effective diffusion coefficient of 1.8×10^{-8} cm^2/sec. An example of the change in thermal desorption spectra versus cathodic overpotential with respect to reversible hydrogen in shown in Fig. 4. The area under the thermal desorption peak is proportional to the diffusible and trapped hydrogen absorbed under each charging condition. Such analysis was performed across a broad range of potentials.

Regarding global hydrogen ingress in 5 M sulfuric acid plus dissolved metal ions, C_H is greatest at potentials cathodic to the reversible H potential as expected (Figure 5). Hydrogen concentration is seen to increase exponentially with hydrogen overpotential (Figure 5). For instance; uptake at a charging potential of -1.10 V$_{Hg/Hg2SO4}$ is 40 times greater than uncharged levels (uncharged levels were a fraction of a wppm). It is interesting to note that H absorption is observed above the reversible H potential. Fig. 5 also illustrates that considerable H uptake could occur in pits or crevices when ohmic voltage drop places the pit surface at a potential of, for instance, -0.75 V even if the pit mouth were polarized to a more positive potential. The scatter bars in the TDS results shown in Figure 5 were determined by analyzing multiple samples charged in the same bulk solution under the same electrochemical conditions. The hydrogen concentration measured reflects the global hydrogen concentration and is not surface sensitive. The global hydrogen concentration data as a function of potential (Figure 5) were fit with an

exponential expression to relate normalized hydrogen concentration ($C_H/C_{H,unch}$) to true charging potential and was valid over the experimental range of -0.15 to -1.2 V $_{Hg/Hg_2SO_4}$:

$$(C_H/C_{H,unch}) = (0.35)\exp(-3.95 \times E_{true}) \qquad [Eq. 4]$$

where C_H and $C_{H,unch}$ are the hydrogen concentrations for charged and uncharged specimens, respectively, with units of g H/g alloy, and E_{true} is in Volts. Using this equation, a sample held at a potential of –0.35 V $_{Hg/Hg_2SO_4}$ would have a normalized hydrogen concentration of 1.4 ± 0.2, i.e., the sample would contain 1.4 ± 0.2 times the amount of hydrogen of an uncharged sample. A sample held at a potential of –1.2 V $_{Hg/Hg_2SO_4}$ would have a normalized hydrogen concentration of 40.1 ± 5.2 times an uncharged specimen.

Figure 5 also reports the charge associated with hydrogen production (e.g., H_2 charge) as a function of potential. Good agreement is seen between the three methods used to asses the charge for a time period equal to the "saturation time" required to obtain a uniform hydrogen concentration within the steel assuming Fickian diffusion and D_{eff} of 1.9 x10^{-8} cm^2/sec at 25°C. A semi-logarithmic relationship is observed between accumulated H_2 charge and H_2 overpotential. It can be seen that H_2 is produced at both overpotentials and underpotentials as expected.

Hydrogen concentration as a function of charging potential for the PH 13-8 Mo exposed to 0.1 M HCl is shown in Figure 6. These data show a similar trend to that seen for 5 M sulfuric acid plus dissolved metal salts. Specifically, hydrogen uptake on an IR-free planar electrode is low near and above the reversible hydrogen potential in the passive region. Uptake occurs globally under cathodic polarization and locally after anodic polarization above pitting thresholds when acid pits are formed. Hydrogen uptake under cathodic polarization in 0.1 M HCl is significantly greater than seen in 5 M H_2SO_4 with metal salts. For instance, C_H reaches 300 times the as-received levels at -1.0V$_{SCE}$. A fit of the data containing the cathodically polarized samples produced the following relationship over the range of potentials -0.15 to -1.0 V$_{SCE}$:

$$(C_H/C_{H,unch}) = (0.93)\exp(-5.9 \times E_{true}) \qquad [Eq. 5]$$

where C_H and $C_{H,unch}$ are again in g H/ g alloy and E_{true} is in volts versus SCE. According to Equation 5, a sample held at a potential of -0.50 V_{SCE} would have a hydrogen concentration 17.8 $\pm$ 2 times that of an uncharged specimen. A specimen held at -1.2 V_{SCE} would have a hydrogen concentration 1105 $\pm$ 144 times the hydrogen concentration of an uncharged sample. This is markedly greater than for samples charged in sulfuric acid plus dissolved metal ions. From Equation 5, a sample charged at -1.599 V_{Hg/Hg_2SO_4} (equivalent to -1.2 V_{SCE}) would only have a hydrogen concentration of 194 $\pm$ 25 times an uncharged specimen.

The fact that absorbed hydrogen concentration also is elevated for samples charged above the pitting potential ($E_{pit} = 0.05$ V_{SCE}), as shown in Figure 7, confirms that hydrogen production and entry occurs in acid pits. A sample charged at an applied potential 150 mV above the pitting potential exhibited a relative hydrogen concentration slightly higher than that of a sample charged at a true potential of 150 mV below the reversible hydrogen potential.[1]

3.3 Near Surface Hydrogen Uptake on Planar Electrodes as a Function of IR-Corrected Potential

Results of nuclear reaction analysis (NRA) of planar electrodes charged at open circuit potential ($\sim -.790$ $V_{Hg/Hg2SO4}$), -0.35 $V_{Hg/Hg2SO4}$ and -1.2 $V_{Hg/Hg2SO4}$ (cathodically polarized) for 10 hours in 5 M sulfuric acid plus dissolved metal ions can be seen in Figure 8. From inspection of Figure 8, low, intermediate and high global C_H values are expected, respectively. In this charging period, hydrogen penetrates to at depth of at least 270 μm assuming Fickian diffusion with a $D_{eff}^H = 1.9 \times 10^{-8}$ cm^2/s. H/total atom ratio was calculated from γ-ray yield as a function of specimen depth. For both samples, the hydrogen concentration measured by NRA for an uncharged, cleaned specimen was subtracted from the data presented in Figure 8 so that only hydrogen due to charging at the three potentials is represented. The results after cathodic polarization show a negligible H concentration profile as expected because the global hydrogen concentration obtained from TDS for -1.2 $V_{Hg/Hg2SO4}$ polarization is far below the detection limit of NRA (ca. $<10^{-3}$ H atoms/total atoms).[29] However, Figure 8 illustrates a local near-surface H/total atom ratio of >0.04 that remains above 0.01 until a depth of approximately 0.25 μm for

---

[1] Anodically polarized samples which pitted experienced local hydrogen uptake which was normalized in a conventional manner to the entire specimen mass. Normalization by a small area surrounding each pit was not attempted but clearly would result in a 10-100 fold increase in the local hydrogen concentration.

samples charged at open circuit potential as compared to samples charged for the same time period at -1.2 $V_{Hg/Hg2SO4}$. Recall that the sample charged at open circuit exhibited much more extensive metal dissolution compared to the cathodically polarized sample yet was polarized below the reversible hydrogen potential (Figure 5). In contrast, the sample polarized at -0.35 V was above the reversible hydrogen potential and within the passive range. All samples show a high surface hydrogen concentration at analysis depths less than 0.02 μm (20 nm) that could be associated with surface hydrogen contamination, as often seen in NRA. This near surface peak was observed on both nitric acid and methanol cleaned samples never exposed to hydrogen at high fugacity. However, the hydrogen concentration for the sample charged at -1.2 $V_{Hg/Hg2SO4}$ rapidly decreased towards the lower detection limit at a depth between 0.02-0.05 μm below the exposed sample surface suggestive of surface hydrogen, possibly in the form of an hydroxide layer. In contrast, the hydrogen concentration for the sample charged at OCP remained significantly higher through 0.30 μm of depth. This is inconsistent with surface contamination. A H/metal atom ratio of 0.01 corresponds to about 216 wppm of H. Hence, near surface hydrogen concentrations with concurrent dissolution and hydrogen production may exceed 1000 wppm with 0.35 um of the planar surface that was exposed to high hydrogen fugacity and simultaneous metal dissolution.

3.4 Pit Scaling Relations and H Uptake in Rescaled Model Pits

Pit rescaling was undertaken for PH 13-8 Mo in 5 M sulfuric acid plus dissolved metal ions to facilitate manufacture of rescaled occluded site that enabled spatially resolved hydrogen measurements. Figure 9 shows the E-logi data used as derived from 5 M H_2SO_4. An example of local potential profiles calculated using the crevice modeling program (*CREVICERv2*) is shown in Fig. 10 at an applied potential (E_{app}) of -0.475 $V_{Hg/Hg2SO4}$. The electrochemical parameters used in the model are shown in Fig. 9. Fig. 10 shows that the locally computed potential, E, is equivalent to the applied potential, E_{app}, at the crevice mouth. However, ohmic potential drop decreases the locally computed potential towards the deaerated OCP with increasing depth within the crevice. This occurs over shallower depths as the crevice mouth dimension (gap) decreases. The local potential drops below $E_{H/H+}$ at $x_{crit1} = x_{HER}$ and reaches the primary passivation potential, E_{pass}, at a further depth $x_{crit2} = x_{Pass}$. The applied potential at the mouth of a crevice is also an important factor (Figure 11). When E_{app} is raised to higher levels, the position

of x_{crit1} associated with potential drop below $E_{H/H+}$ is shifted towards deeper positions in the crevice assuming fixed chemistry which is likely in the case of the concentrated metal salt solution. Similarly, $x_{crit2} = x_{Pass}$ is shifted towards deeper depths when E_{app} is raised. The opposite effect is seen when E_{app} is lowered. Thus, beyond a critical depth given by $x > x_{crit1}$, a passive stainless steel is subjected to net H production, but remains in the passive state. When the local potential drops far enough, the material undergoes a passive-active transition and net H production is thermodynamically favorable on the actively dissolving surface (e.g., $x > x_{crit2}$). From these results, relationships for two critical distances from the mouth of the crevice were developed that apply to the selected potentials. The first critical distance is the distance from the crevice mouth at which the pit potential equals $E_{H/H+}$, $x_{crit1}(E_{H/H+}) = x_{HER}$. The second critical distance, $x_{crit2}(E_{pass})$, was designated as the distance from the mouth of the crevice where the local crevice potential drops to E_{pass}.

Figs. 12 and 13 show the corresponding anodic and cathodic half-cell reaction rates versus depth x. The anodic reaction rate peaks due to the active polarization nose (Figure 1 and 9) while the HER rate increases with potential decrease (Figure 3), and levels at the OCP of the pit bottom. However, i_{an} can decrease with pit depth, as the active polarization curve indicates, when potentials reach the OCP of the pit. The relationship between x_{crit1}, x_{crit2} and G for PH 13-8 Mo in 5 M H_2SO_4 plus metal salts are shown in Fig. 14. The square of each critical distance is, indeed, a linear function of G to very good approximation. A plot of x versus G (not shown) is not linear, confirming that x^2/G is the correct geometrical scaling relationship for both the case of H the passive-to-active transition modeled here. The x-G relation is critical to translating actual pits of micron scale to manufactured pits of millimeter scale.[20,26] Guided by Fig. 14, model pits/crevices of millimeter scale (e.g., 1500 μm inside cylindrical diameter (G) and 40 mm length, x) were produced using PH 13-8 Mo. Fig. 14 shows that this is equivalent to a 60 μm diameter crevice with x > 3 mm, etc. It can be seen that rescaled model pits possess x_{crit1} and x_{crit2} over macroscopic lengths from 5-10 mm. Hence, different potential dependent corrosion and H uptake behavior would occur over lengths of millimeters instead of depths of micrometers typical of actual pits. These samples were held in 5 M H_2SO_4 plus dissolved metal ion under potentiostatic control. Local potential was measured versus depth x in rescaled crevices. Potentials were held at potentials ranging from -0.4 to -0.60 $V_{Hg/Hg2SO4}$. IR drop was insufficient at high passive potentials such as -0.40 $V_{Hg/Hg2SO4}$ to produce significant potential drop inside

one-dimensional pits because pits walls exhibited low anodic passive current densities (Figures 1 and 9) near these potentials that did not produce enough ohmic voltage drop to drop the potential below E_{Pass} in order to activate stainless steel surfaces. However, when E_{app} was decreased to -0.60 $V_{Hg/Hg2SO4}$, significant potential drop was seen versus x such that the bottom of the pit approached the limiting or open circuit potential near –0.76 V (Fig. 1-2). Rescaled pit specimens were exposed, removed, rinsed, stored in LN_2 and sectioned radially for H analysis versus depth x. Fig. 15 shows one potential profile experimentally measured using the micro-reference electrode for a sample held in 5M H_2SO_4 plus dissolved metal ions at -0.60 $V_{Hg/Hg2SO4}$ (applied potential) with a 1500 μm inside diameter and 40 mm length. The pit exhibits a 150 mV potential drop from its mouth to its bottom. Most of the potential drop occurs in the first 10 mm of depth, consistent with the modeling results (Fig. 10 and 11). An indication of anodic dissolution as a function of x, is recorded by examining the increase in inside diameter of the pit. This increase in pit diameter indicates increased anodic dissolution as a function of x due to loss of passivity and high dissolution rates in the active E-i region. The decrease in diameter back towards the original value at the pit bottom is consistent with a decrease in i_{an} at the OCP near the bottom of the crevice (Fig. 15).

The decrease in E and increase in i_{ca} produce an increase in C_H with depth in the crevice when the applied potential at the mouth is held at -0.60 $V_{Hg/Hg2SO4}$ (Fig. 15). The local level of C_H within pits increases even when uptake is minimal on external passive surfaces. Independent corroboration is obtained when C_H predicted from the planar electrode studies using an identical solution is plotted at each interfacial potential recorded using the microelectrode (Fig. 15). The predicted values from a combination of bulk electrode studies and local potential measurements are consistent with TDS measured values. The local C_H within the model pit increases nearly 100% from approximately 4 times an uncharged specimen near the pit mouth to almost 7 times that of an uncharged specimen at x greater than 10 mm within the pit where potential is lowest and cathodic current density is at its highest value. Therefore, a planar electrode held just in the passive region at –0.6 V would be expected to produce and concentrate H in pits or crevices at depths greater than $x > x_{HER}$.

The analysis described can be repeated at various E_{app} to provide indication of the potential and depth, x, dependency of C_H as a function of x for occluded sites of selected geometries. In limited testing, other anodic and cathodic potentials were applied to rescaled pits. Microelectrode measurements were performed in conjunction with hydrogen analysis. At an externally applied potential of -0.20 V $_{Hg/Hg_2SO_4}$ in the passive range, very little H was measured. However, a few high measurements were recorded in sections which contained pit sites. Figure 16 shows the results for the same model pit geometry as Figure 15, with an externally cathodic applied potential of -1.2 V $_{Hg/Hg_2SO_4}$ (cathodic). The local potential measured within the rescaled pit increases to the open circuit potential beyond a critical depth and the measured hydrogen profile is in agreement with the calculated hydrogen profile using data obtained using the data base from the bulk electrode experiments (Figure 5). Higher hydrogen concentrations were measured at more negative (more cathodic) local potentials as expected from the bulk electrode experiments. Under cathodic polarization, higher levels of cathodic polarization are achieved near the pit mouth and the level of polarization decreases with pit depth. In this case, C_H is greatest at smaller x. Examination of the cathodic current density as a function of measured potential within the pit shows a decrease in current density with increasing x to a final value of approximately 3×10^{-3} A/cm^2 in the first 5 mm of crevice depth.

4. DISCUSSION

Global and Local Surface Hydrogen Uptake on Planar Electrodes

_____Steady state global hydrogen concentrations in a Fe-13Cr-8Ni-2Mo-1Al alloy (i.e., potential dependent effective solubilities) were enhanced as an exponential function of hydrogen overpotential in both 0.1 M HCl and H$_2$SO$_4$ plus concentrated metal ions (Figures 5 and 6). Hydrogen uptake was also seen in pitted samples in 0.1 M HCl (Figure 7). However, pits deviate from IR free planar electrodes and rescaled pits enabled quantification. Such a exponential dependency may be predicted between the interfacial potential at a pit bottom and steady state effective hydrogen solubility using the theory of electrochemical hydrogen absorption and solubility in metals. The operative HER mechanism for steels with comparable Tafel slopes is coupled discharge-chemical recombination.[21] This reaction mechanism occurs in two steps[30]:

$$1) \quad H^+ + e^- + M \xrightarrow{k_1} M - H_{ads} \qquad\qquad [Eq. 6]$$

$$(2) \quad M - H_{ads} + M - H_{ads} \xrightarrow{\quad k_2 \quad} 2M + H_2 \qquad \text{[Eq. 7]}$$
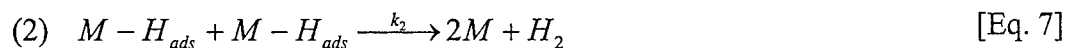
The hydrogen fugacity experienced at the metal/electrolyte interface for this mechanism is related to cathodic overpotential according to[30]

$$f_{H_2} = 10^{1.5} \exp\left(\frac{-\eta F}{2RT}\right) \qquad \text{[Eq. 8]}$$

Hydrogen dissolves in metals according to the following additional step which occurs in competition with the second step shown in Eq. 7 above:[30]

$$(3) \quad 2H = 2M\text{-}H_{ads} = 2M\text{-}H_{diss} \qquad \text{[Eq. 9]}$$

Where H_{ads} is atomic hydrogen adsorbed on the surface of the metal and H_{diss} is atomic hydrogen that has dissolved into the metal either interstitially or through atomic vacancies. The expression describing the equilibrium perfect lattice interstitial concentration in equilibrium with a give hydrogen pressure can be represented by:[30,31]

$$C_o = K_{eq} \, p^{1/2} = 0.00185 p^{1/2} \exp(-28.6 kJ / mole / RT) \qquad \text{[Eq. 10]}$$

where K_{eq} is the equilibrium constant for the nearly perfect lattice hydrogen solubility in iron; $K_{eq}= 0.00185\exp(-28.6 \text{ kJ/mole/} RT)$, C_o is the concentration of lattice-dissolved atomic hydrogen, p is the sensible pressure of H_2 gas such as in gas phase charging, R is the ideal gas constant and T is the temperature. The sensible pressure of hydrogen gas is related to electrochemical hydrogen fugacity.[2],[32] Assuming that fugacity is directly proportional to pressure at low overpotentials, then the lattice dissolved atomic hydrogen concentration for the coupled discharge-chemical recombination reaction mechanism can be described as:

$$C_o \propto K_{eq}\left(10^{0.75}\right)\exp\left(\frac{-\eta F}{4RT}\right) \qquad \text{[Eq. 11]}$$

where K_{eq} is described above, F is Faraday's constant and R and T have been defined above. Since η is negative, increasing the hydrogen overpotential must therefore increase the amount of dissolved hydrogen in the material exponentially. However, the quantity of hydrogen, C_H, actually measured in the TDS method and reported in Figures 5, 6 and 7 reflects the total hydrogen concentration, C_{Htot}, (e.g., includes the sum of lattice, c_o, and trapped $C_{H,trap}$,

---

[2] The assumption that fugacity is directly proportional to pressure is only valid at low pressures or for ideal gases.

hydrogen). Assuming that the trapped hydrogen concentration is proportional to the lattice hydrogen concentration as well as the trap strength through a Boltzmann type expression and that $C_{H,trap} \gg C_o$, the following relationship describes the relationship between C_o, the concentration of lattice-dissolved atomic hydrogen and C_H,trap.

Recall that C_o is an exponential function of hydrogen overpotential as indicated in Eq. 11:

$$C_{Htrap} = \left. C_O \exp\left(\frac{E_B}{RT}\right) \middle/ 1 + C_O \exp\left(\frac{E}{RT}\right) \right.$$

[Eq. 12]

In this expression, E_B is the trap binding energy: in this case the binding energy associated with the dominating broad TDS peak indicating a trap state in the TDS data around 450 K (Figure 4). An exponential relationship between $C_H/C_{H,unch}$ and E_{true} is seen in Figures 5 and 6. Equation 12 produces an relationship that is quite consistent with these experimental findings when potential dependent values of C_o from Eq. 11 are inserted into Eq. 12. For instance, Eq 12 predicts a 450 fold increase in $C_{Htrap} \sim C_{Htot}$ at 25°C assuming $E_B = 12$ kJ/mol when the hydrogen overpotential is increased on the steel from 0 to about 480 mV (e.g., -780 mV $_{SCE}$) in 0.1 M HCl. Such an increase is in reasonable agreement with Figure 6 and suggests that Eq. 12 is a valid expression describing the relationship between $C_{H,trap}$ and C_o and, therefore, $C_{H,trap}$ and η taking into consideration Eq. 11. The results in experimental $C_{H,trap}$ versus η for H_2SO_4 and metal salts are significantly less than seen in HCl solution despite similar H_2 production rates indicating that the salt film and possible Ni replating limit hydrogen ingress. For example, Ni^{+2}, which has the most noble standard reduction potential of Ni^{2+}, Cr^{3+} and Fe^{2+}, would plate out first at approximately -0.949 V_{Hg/Hg_2SO_4} [43]. Below this potential, reduced nickel on the surface of the alloy may inhibit hydrogen ingress because fcc nickel could serve as a permeation barrier.

Local Hydrogen Uptake

The NRA results of Figure 8 indicate a high local total hydrogen concentration at the surface of the specimen exposed at the open circuit potential in 5 M H_2SO_4 plus dissolved metal ions. This concentration profile extended to a depth of almost 0.35 µm (350 nm). This depth

exceeds likely oxide film[33] and selectively dissolved metallic film thicknesses[3] but does not extend to the full depth to which diffusible hydrogen might penetrate by Fickian diffusion processes (i.e., ~300 μm) during the 10 h charging period. It is likely that a lower concentration of diffusible hydrogen penetrates well beyond a 0.35 μm depth but that such a global concentration of hydrogen is below the detection limit of the NRA method. On the other hand, TDS measurements conducted on mm thick specimens under the same conditions as NRA studies would have difficulty detecting the locally high hydrogen concentrations detected by NRA owing to the fact that specimen thicknesses used in planar electrode tests exceed the thin layer detected by NRA by many orders of magnitude. Thus NRA results detect high near surface hydrogen concentrations within tens of microns of the charging surface that are not detected by TDS. In contrast, TDS is not a surface sensitive technique that would sense high local hydrogen levels within hundreds of nm of the sample surface, it would report the average of such high local surface concentrations over the entire sample thickness. In combination, rescaled crevices would enable TDS measurements over mm length scales that represent micrometers in real crevices and enables NRA measurements which have great depth sensitivity but poor lateral resolution limiting its use in real pits and cracks.

The near surface H concentration profile produced from NRA is not consistent with Fickian transport of diffusible hydrogen. In summary, two possibilities exist: that high detected levels of local near-surface hydrogen reside in both lattice and trapped sites in the alloy or that high levels of detected near-surface hydrogen are present in some other state (i.e., such as OH⁻ present in oxide films or dealloyed layers) that is not actually hydrogen within the bulk metal. The latter is not supported by layer thickness estimates in the literature associated with selective dissolution (dealloying) below the parting limit[34]. High hydrogen concentrations within the bulk metallic phase would be hard to attribute to lattice solubility alone because the electrochemical fugacity within active pits, albeit high, does not necessarily support such equilibrium concentrations assuming that the perfect lattice solubility of hydrogen in PH 13-8 Mo is similar to that in iron[35] and the normal density of trap sites in such steels.[25] This is especially true near OCP where the hydrogen overpotential is less than 100 mV.

---

[3] One explanation is that the high hydrogen concentration detected by NRA is hydrogen associated with OH⁻ in a passive or dealloyed layer instead of atomic hydrogen in solid solution at lattice or in clustered trap sites. In order for this to be possible the oxide film on the corroded surface and /or the dealloyed layer would have to reach thicknesses of 0.35 um which appears unlikely given that typical oxide and dealloyed layer thicknesses (below the parting limit) are often restricted to less than 100 nm (0.1 μm).

One other explanation is that high concentration hydrogen-vacancy or divacany trap-like complexes are formed at corroding surfaces and that these account for a very high near-surface hydrogen concentration not seen at equilibrium or normal quenched in vacancy concentrations. This process would be speculated to occur via vacancy injection via incongruent or selective alloying element dissolution concurrent with hydrogen production. This scenario would produce abnormally high hydrogen concentrations restricted to limited surface regions. Such non-Fickian hydrogen concentration profiles would not be altered by hydrogen diffusion into the specimen bulk because of the relative immobility of the vacancy clusters. Few prior experiments have reported direct evidence of such a result, possibly because techniques with high spatial resolution have only recently become available and applied to H uptake in electrochemical charging at occluded sites.[36] However, high room temperature hydrogen concentrations recently have been observed in electrochemically charged Al[37,38] and at Al crack tips.[36] Little evidence of this phenomenon has been reported in bcc stainless steel prior to this publication.

Hydrogen Uptake in Occluded Sites

PH 13-8 Mo exhibits an active-passive transition in a simulated pit/crevice solution. Moreover, this alloy exhibits a deaerated OCP below $E_{H/H+}$ (Figure. 1). Given this behavior, there are a variety of ways that an anodically polarized pit, crevice or crack that experiences IR drop, acidification and O_2 depletion could lead to H uptake under conditions where boldly exposed planar PH 13-8 Mo surfaces would be expected to remain passive and above $E_{H/H+}$. H uptake was observed in 5 M H_2SO_4 + dissolved metal salts at the deaerated OCP (Fig. 5) as well as when a rescaled pit was held in at −0.6 V in the passive region (Figure 15). Here, ohmic voltage drop decreased the local potential below $E_{H/H+}$ at $x > x_{HER}$ even though the applied potential at the mouth of the occluded site was above the passivation potential. These data help to explain the finding that PH stainless steels are susceptible to H embrittlement at OCP or under anodic polarization in chloride solutions, especially when pitting or crevice corrosion occurs leading to acidification.[39,40] H production has also been observed in model pits in iron,[41] carbon steel[41] and a duplex stainless steel[42] when $x > x_{HER}$ despite external polarization to noble potentials in the passive region. H uptake has also been reported in the literature during permeation experiments on anodically polarized planar electrodes[43] under pitting conditions,[44] as well as during intergranular corrosion.[45] At issue here is accurate quantification of local H

concentrations in such corrosion sites. The use of rescaled occluded sites in conjunction with NRA and TDS measurement of hydrogen concentration provides the opportunity for greater quantification of H levels over a range of applied potentials.

Ultimately, C_H values determined in this manner could be compared to C_{Hcrit} values that produce a large drop in K_{Ic}. This would enable determination of the potential dependency of HEAC susceptibility. In this alloy, and similar Cr-containing high strength precipitation age hardened stainless steels, both external anodic and cathodic polarization cause a decrease in K_{th} (Figure 17). The result is interpreted through increases in hydrogen uptake upon cathodic polarization as well as both IR drop and crack tip acidification in the case of anodic polarization. Moreover, the potential, chemical and x^2/G combinations that produce HEAC could be predicted from identification of the combinations of conditions where $C_H > C_{Hcrit}$. Hence, such a potential dependency could be predicted. The rescaled crevice data above supports this notion. Embrittlement is expected upon cathodic polarization but also would be expected upon anodic polarization depending on acidification and IR drop that lowers $E < E_{H/H+}$ at $x > x_{crit1}$. Moreover, it could be predicted whether electrochemically long or short cracks might be more prone to HEAC in the case where local hydrogen uptake at the occluded site dominates over bulk specimen charging. Note that local hydrogen uptake is likely more important for complex high strength materials with low D_{eff} such as the PH 13-8 Mo steel discussed here because rapid diffusion away from a local site of locally high hydrogen concentration is not possible given slow long range Fickian diffusion. These preliminary results suggest that electrochemically short cracks might be of greater concern than electrochemically long cracks when external cathodic polarization is extensive because the crack tip would be located at a position near the surface where C_H is greater. However, long cracks might lead to higher levels of C_H when anodic polarization prevails because the ohmic potential drop lowers the interfacial potential below $E_{H/H+}$ when $x > x_{crit1}$ which is possible in deep cracks. Evidence is being collected to support or refute this assertion using long and short crack data.

Utilization of crevice scaling laws to rescale occluded sites when considering various critical potentials

Modeling shows that IR drop in a crevice can produce local crevice potentials that enable activation of an anodically polarized metal surface within the crevice concurrent with H

production and uptake (Figures 10 and 11). The relationship $x^2/G = constant$ applies for E_{pass} and E_{H/H^+} albeit with different constants (Figure 14). Thus, the notion of a critical potential can be applied to hydrogen embrittlement as well as crevice corrosion. Such scaling relationships have been seen before;[22,26,26,27] the exact values of the constant in this paper are specific to PH 13-8 Mo under the conditions studied. The $x^2/G = constant$ relationship has been previously used to describe depassivation and activation phenomena of concern in crevice corrosion (i.e., IR* model of Pickering).[22,28,41,42] In this study both x_{crit1} and x_{crit2} have been specified, although such relations should hold at any potential of interest. Different regimes have been identified for crevices or pits in PH 13-8 Mo. Under anodic polarization, there is a combination of x and G in a crevice or crack where the stainless steel would be passive and remain above E_{H/H^+}, a region where H production could occur but not activation, and a deep crevice depth (x_{crit2}) beyond which both activation and net H production occur. Here, H absorption was greatest (Fig. 5), charging efficiency was greatest and nuclear reaction analysis indicated very high local hydrogen concentrations within fractions of micrometer depths from a corroding surface undergoing concurrent hydrogen production. A variety of alloys could exhibit such generic behavior albeit with different details. The requirements include pit susceptibility, a passive-to-active transition in a solution analogous to the pit solution, an OCP in the active deaerated state that is below the E_{H/H^+} and $x>x_{HER}$ at appropriate G. The relationship described can provide guidance for construction of model pits of a large enough scale to measure local potentials and C_H electrochemically identical to an actual crevice of micrometer scale. Such a real crevice would be too small for interrogation to obtain C_H values. The model pit results in Figures 10-15 show that H uptake can occur under conditions where the rescaled pit mouth is held in the passive range when $x>x_{crit}$. The local C_H values (with mm scale spatial resolution) increase to 7 times the value in an uncharged specimen exposed to humid air and the behavior versus x could not be predicted from global H measurements alone on planar specimens containing pits or crevices (Figure 15).

5. CONCLUSIONS

The effects of occluded site (e.g., pit or crevice) geometry and electrochemical conditions on local hydrogen production and uptake in a precipitation age-hardened Fe-13Cr-8Ni-2Mo-1Al stainless steel (PH 13-8 Mo) were explored. On planar electrode surfaces that did not contain

intentional occluded sites, the total hydrogen concentration was found to increase exponentially with increasingly negative true interfacial potential. This finding was shown to be consistent with electrochemical theory of hydrogen absorption using the coupled discharge-chemical recombination hydrogen evolution reaction mechanism. The effective hydrogen solubility at each hydrogen overpotential was greater in 0.1 M HCl solution compared to a simulated pit solution comprising of 5 M sulfuric acid plus dissolved metal ions. Anodic polarization and subsequent pitting created elevated hydrogen levels in the case of 0.1 M HCl solutions as the pit bottom was rationalize to fall below the reversible hydrogen potential. High levels of near-surface hydrogen uptake was observed under conditions where joint uptake and dissolution occurred.

Crevice scaling laws were used to rescale pits to sizes that enable spatially resolved quantification of local H concentrations as a function of both E_{app} and pit depth. Separate scaling relationships of the form x^2/G described the relation between the critical depth to achieve both passive-to-active potentials and E_{H/H^+} as a function of the gap (G) associated with the occluded site. Exposure of a PH stainless steel to a simulated pit chemistry confirms that H uptake occurs locally on anodically polarized planar electrodes whose surfaces are polarized in the passive range when containing an occluded site. Specifically uptake occurred at occluded site depths such that the condition $x > x_{HER}$ is met. Such occluded sites experience sufficient IR drop to shift local potentials below E_{H/H^+} even when external surfaces are polarized to passive potentials. The rescaling technique can be applied to study HEAC susceptibility versus applied potential for various occluded site geometries.

External anodic polarization resulted in hydrogen ingress which increased at depths in the occluded site where $x > x_{HER}$. In contrast, external cathodic polarization, such that the interfacial potential was more negative than E_{H/H^+} at the mouth of the occluded site, produced greater levels of hydrogen ingress at small values of x. These results suggest that electrochemically short cracks may experience a greater extent of hydrogen uptake when subjected to net cathodic polarization but that electrochemically long cracks would be more deleterious in the case of anodic polarization in situations where local hydrogen uptake at the occluded site is favored over bulk charging.

6. ACKNOWLEDGMENTS

LIST OF FIGURES

Figure 11. Potential versus depth data for various externally applied potentials at the mouth of a square prism shaped crevice as determined by *CREVICERv2* using the 0.1 M sulfuric acid plus dissolved metal ions E-Log(i) curve modified with the 5 M sulfuric acid plus dissolved metal ions E-Log(i) parameters. Gap size = 1000 μm. Solution conductivity = 0.46 mho/cm.

Figure 12. Current density versus depth modeling data for square prism shaped crevice showing (a) i_{anodic} and (b) the absolute value of $i_{cathodic}$. The externally applied potential, E_{app}, was -0.475 $V_{Hg/Hg2SO4}$.

Figure 13. Current density versus depth modeling data for square prism shaped crevice showing (a) i_{anodic} and (b) the absolute value of $i_{cathodic}$. The externally applied potential, E_{app}, was -0.475 $V_{Hg/Hg2SO4}$.

Figure 14. x_{crit2} versus gap data for PH 13-8 Mo. Two x_{crit} parameters are plotted for conditions: $i_{crit} = 10^{-2}$ A/cm^2, $E_{H/H+}$ = -0.59 V Hg/Hg$_2$SO$_4$, E_{pass} = -0.70 V Hg/Hg$_2$SO$_4$, E_{app} = -0.475 V Hg/Hg$_2$SO$_4$.

Figure 15. Potential, C_H and pit diameter versus pit depth from a rescaled experimental pit for a 1500 μm diameter by 40 mm depth cylinder exposed to 5 M H$_2$SO$_4$ + dissolved metal ions. E_{app} = -0.60 V Hg/Hg$_2$SO$_4$

Figure 16. Model pit results for a 1500 um gap and 40 mm depth drilled cylinder in the upright position exposed to 5 M sulfuric acid plus dissolved metal ions. E_{app} = -1.2 $V_{Hg/Hg2SO4}$. $E_{H/H+}$ = -0.59 $V_{Hg/Hg2SO4}$. E_{pass} = -0.70 $V_{Hg/Hg2SO4}$. a) Measured potential, TDS measured C_H, and calculated C_H versus depth.

Figure 17. Normalized threshold stress intensity for hydrogen environment assisted crack initiation of pre-cracked precipitation age hardened martensitic stainless steels as a function of applied potential in 0.6 M NaCl solution. Data shown is for high strength (σ_{ys} = 1476 MPa) PH 13-8 (Fe-13Cr-8Ni-2Mo-1Al) [ref. 22], high strength (σ_{ys} =1220 MPa) PH 17-4 [ref. 17], and high strength (σ_{ys} = 1130 MPa) PH 17-7 (Fe-6%Ni-19%Cr-1%Al-03.%Cu)) [ref. 40].
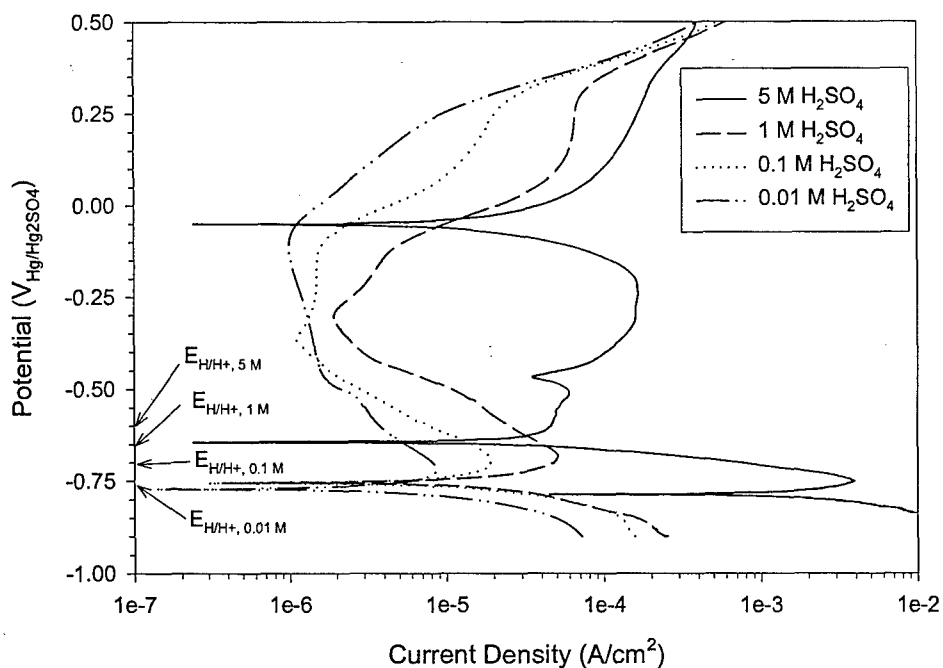
Figure 1. Anodic E-Log(i) data for PH 13-8 Mo stainless steel in the H1050 heat treated condition exposed to various deaerated sulfuric acid plus 0.1 M Fe^{+2}, 0.018 M Cr^{+3} and 0.01 M Ni^{+2} solutions at 25°C. Measurements taken versus a Hg/Hg_2SO_4 electrode.
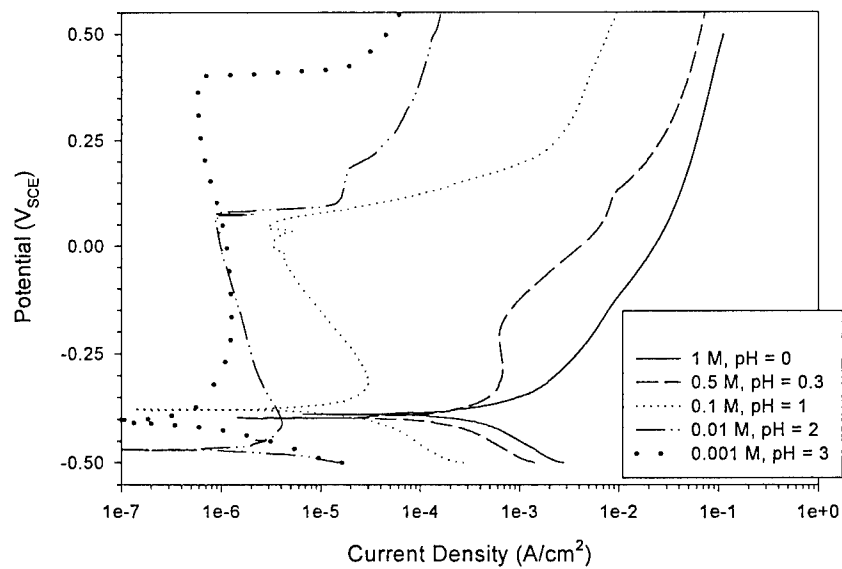
Figure 2. Anodic E-Log(i) data for PH 13-8 Mo stainless steel in the H1050 heat treated condition exposed to various deaerated hydrochloric acid solutions at 25 °C. Measurements taken versus a saturated calomel reference electrode.
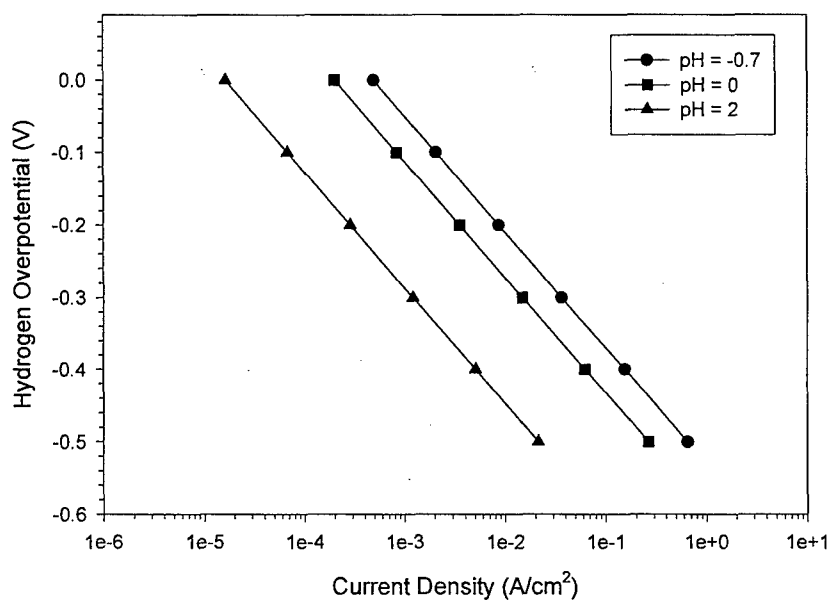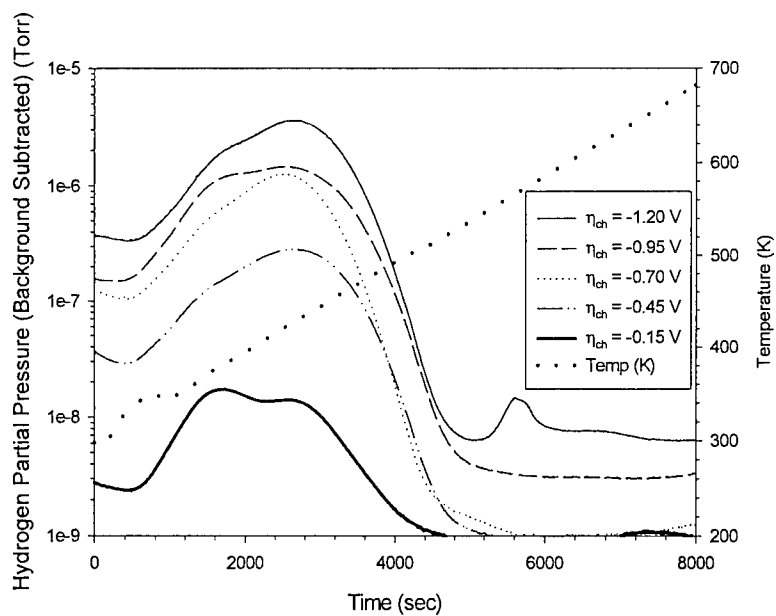
Figure 3. Calculated cathodic hydrogen overpotential versus true cathodic current density, i_{H2}, (from relationship) for PH 13-8 Mo in the H1050 heat treated condition exposed to deaerated sulfuric acid plus 0.1 M Fe^{+2}, 0.018 M Cr^{+3} and 0.01 M Ni^{+2} solutions at 25 $^{\circ}$C.

Figure 4. Hydrogen partial pressure versus time data from outgassing during programmed thermal desorption after exposure to various hydrogen charging overpotentials for PH 13-8 Mo in the H1050 heat treated condition. Samples charged for 1.5 days in 0.1M HCl. Temperature ramp rate is 3 °C/min.
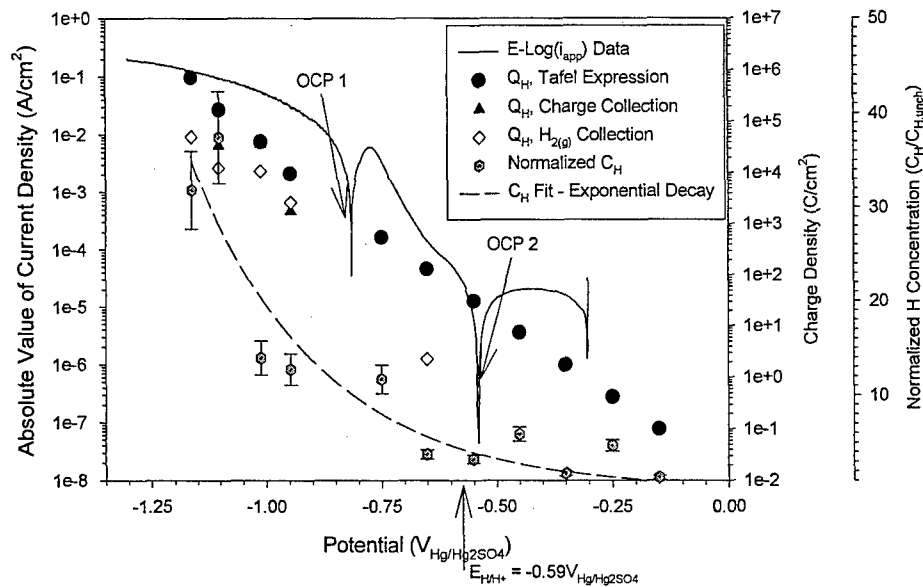
Figure 5. $C_{H,tot}$ obtained from TDS and hydrogen charge densities versus interfacial potential for planar PH 13-8 Mo specimens in the H1050 heat treated condition after charging in deaerated 5 M H_2SO_4 plus dissolved metal ions at 25°C.
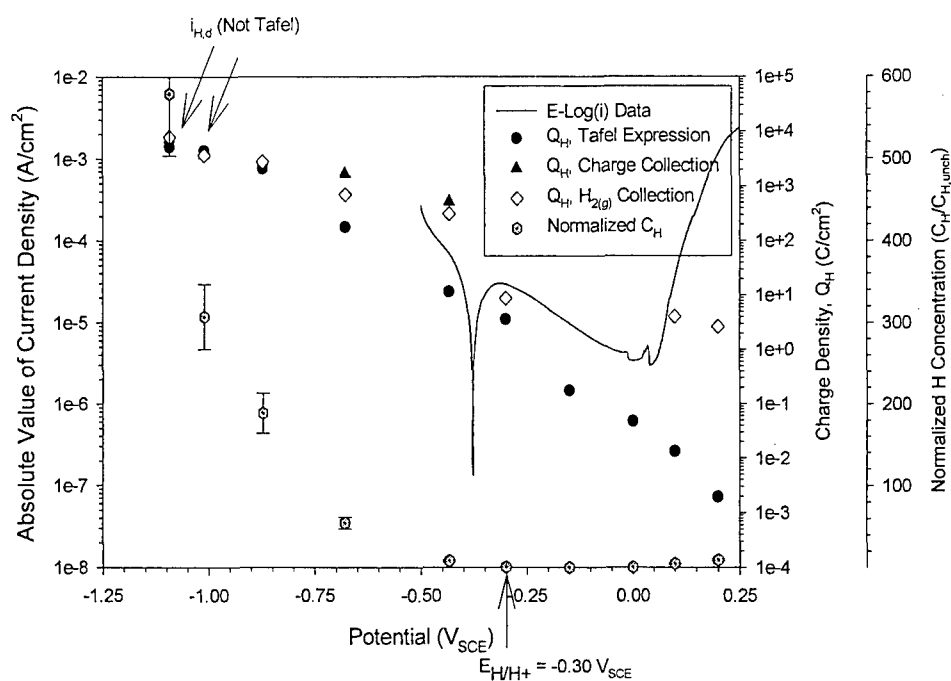
Figure 6. $C_{H,tot}$ obtained from TDS and hydrogen charge densities versus interfacial potential for planar PH 13-8 Mo specimens in the H1050 heat treated condition after charging in deaerated 0.1 M HCl at 25°C.
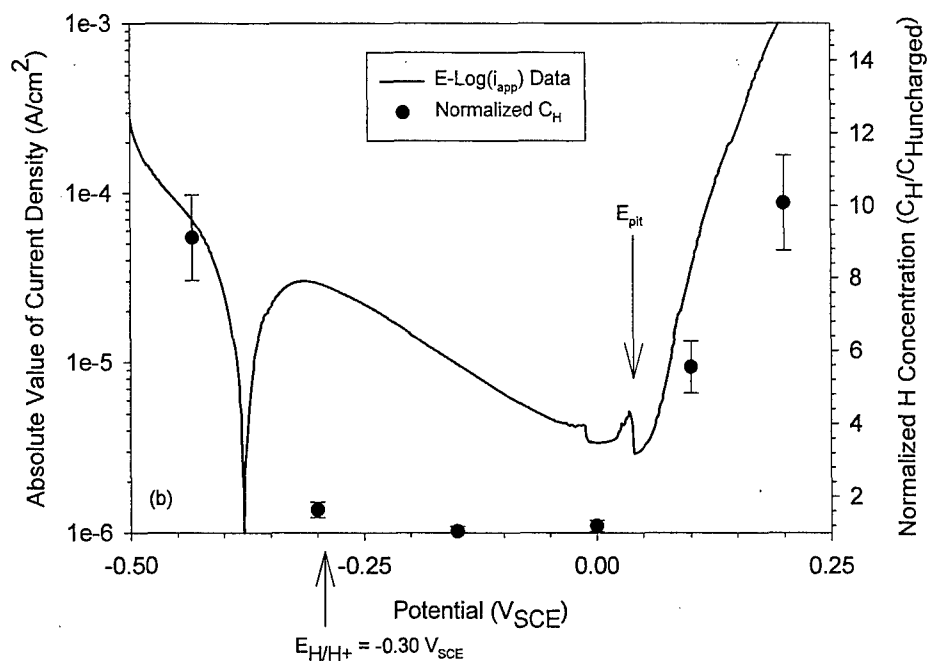
Figure 7. $C_{H,tot}$ obtained from TDS and hydrogen charge densities versus potential for planar PH 13-8 Mo specimens in the H1050 heat treated condition after charging in deaerated 0.1 M HCl at 25°C. Cathodic and anodic data are shown with C_H not normalized to local pit volume in case of data points A and B.
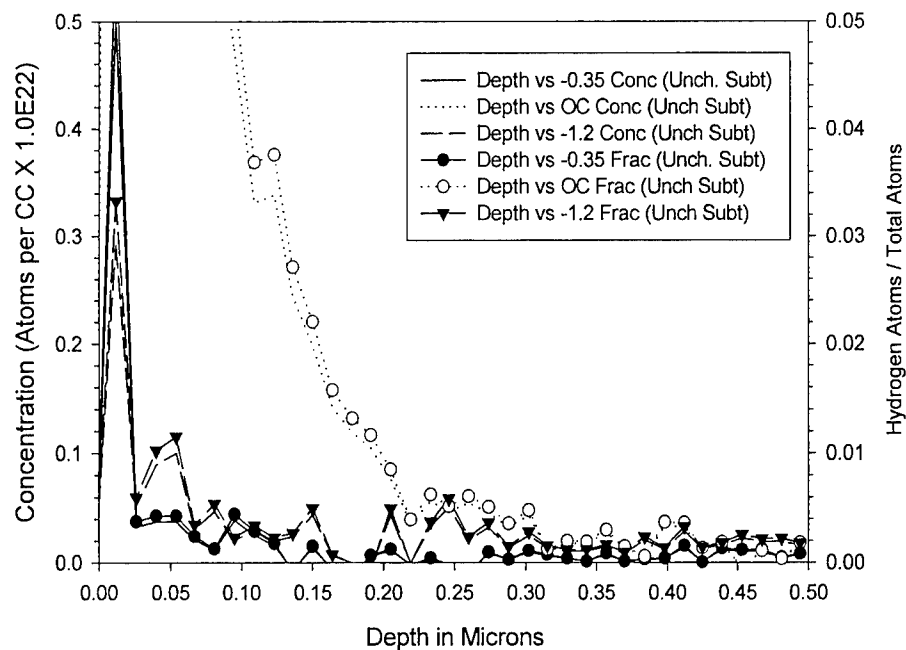
Figure 8. Local total H concentration from NRA versus perpendicular distance from sample surfaces for planar PH 13-8 Mo electrodes charged for 10 hours at OCP, -1.2 $V_{Hg/Hg2SO4}$, and -0.35 V $_{Hg/Hg2SO4}$ in deaerated 5 M H_2SO_4 plus dissolved metal salts at 25 °C. Measurement by nuclear reaction analysis.
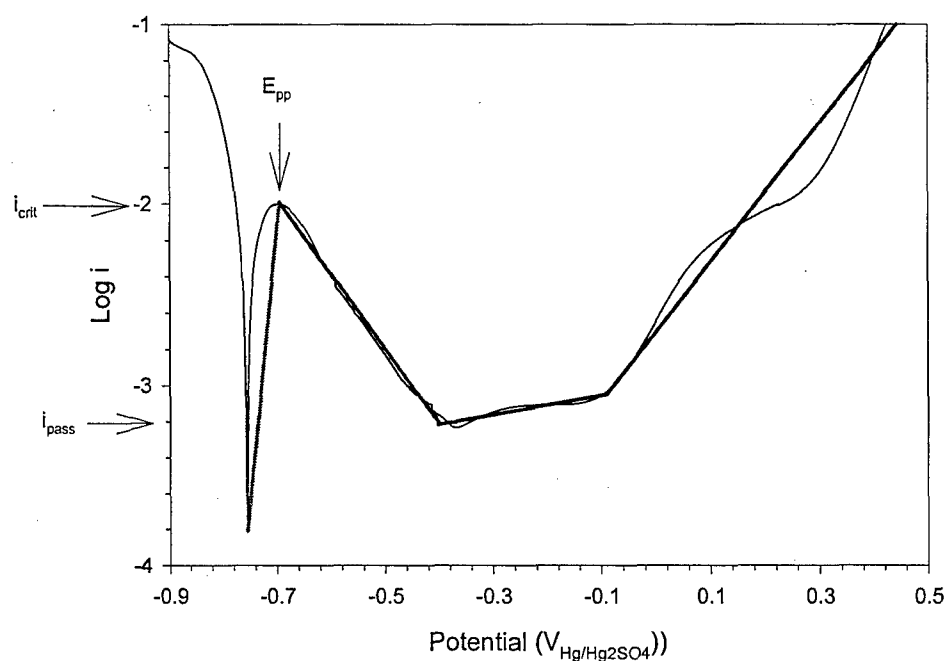
Figure 9. Polarization data entered in CREVICERv2 program. Curved line represents actual polarization data from PH 13-8 Mo exposed to 0.1 M sulfuric acid solutions containing dissolved metal salts and adjusted so that i_{crit}, E_{pp}, and i_{pass} are representative of the 5 M sulfuric acid plus metal salts E-Log(i) data.. Straight-line segments represent linear fit of data entered into CREVICERv2.
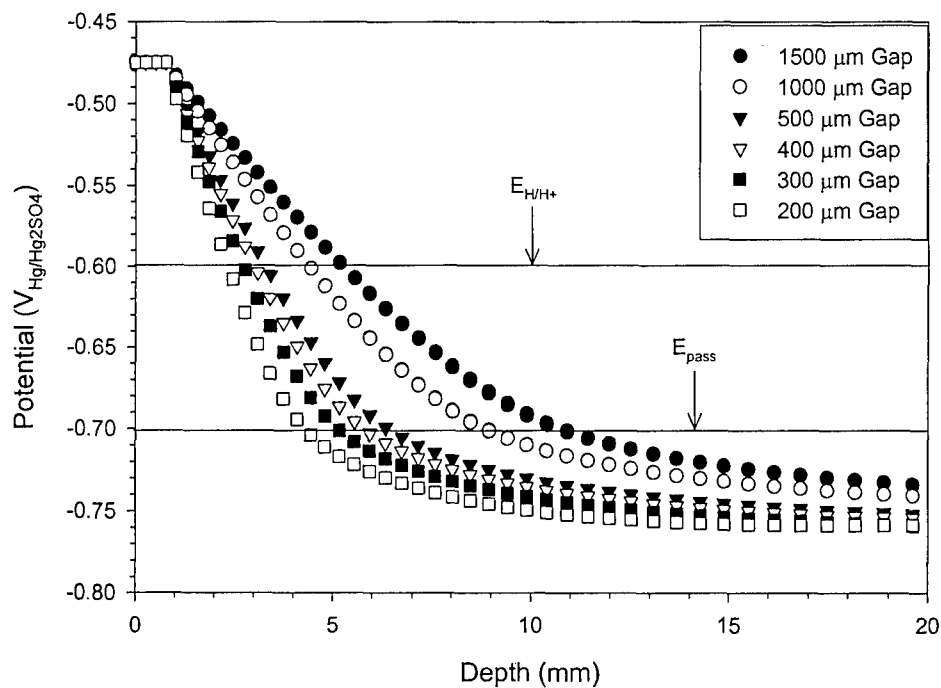
Figure 10. Potential versus depth data using the Fig. 9 E-log(i) data for a square prism shaped crevice as determined by *CREVICERv2* for a square prism shaped crevice at the indicated square gap. Selected externally applied potential (E_{app}) was -0.475 $V_{Hg/Hg2SO4}$.
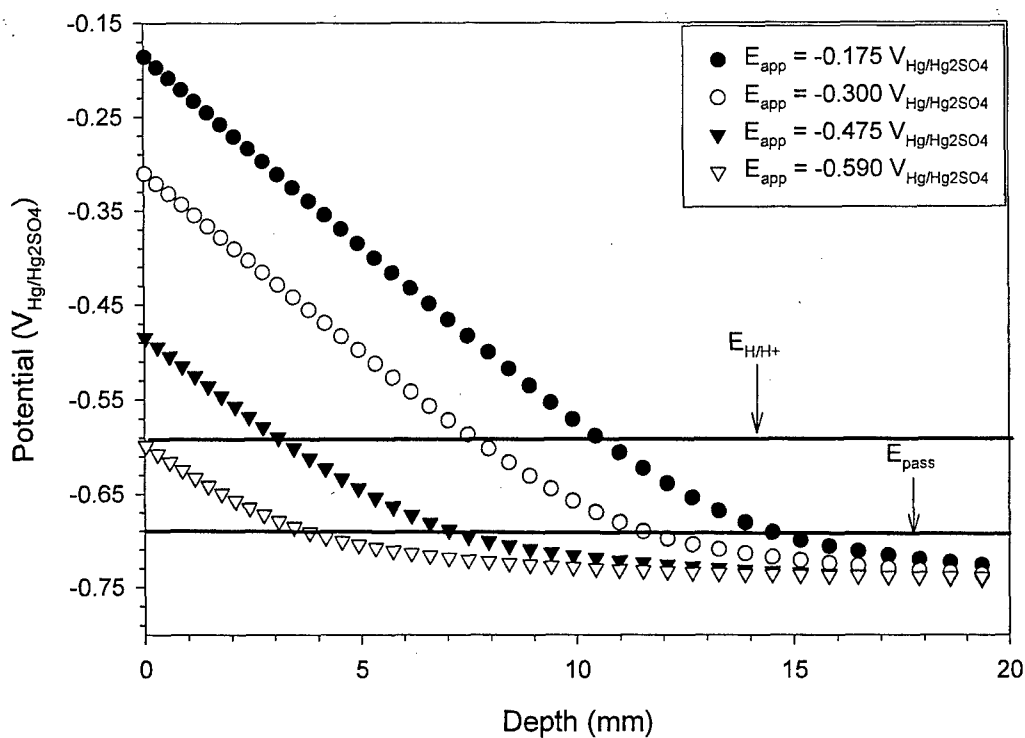
Figure 11. Potential versus depth data for various externally applied potentials at the mouth of a square prism shaped crevice as determined by *CREVICERv2* using the 0.1 M sulfuric acid plus dissolved metal ions E-Log(i) curve modified with the 5 M sulfuric acid plus dissolved metal ions E-Log(i) parameters. Gap size = 1000 μm. Solution conductivity = 0.46 mho/cm.
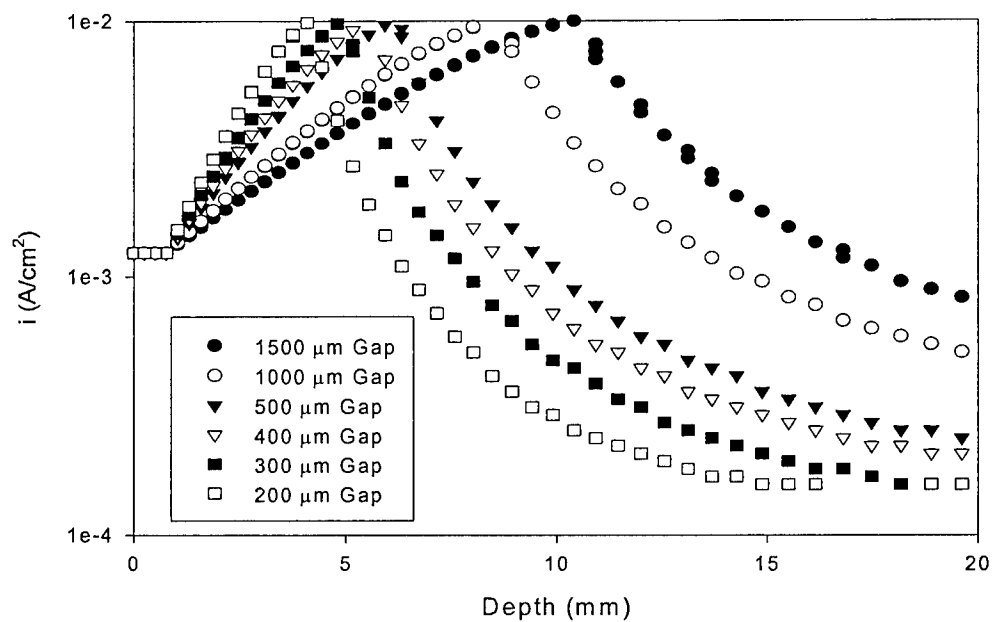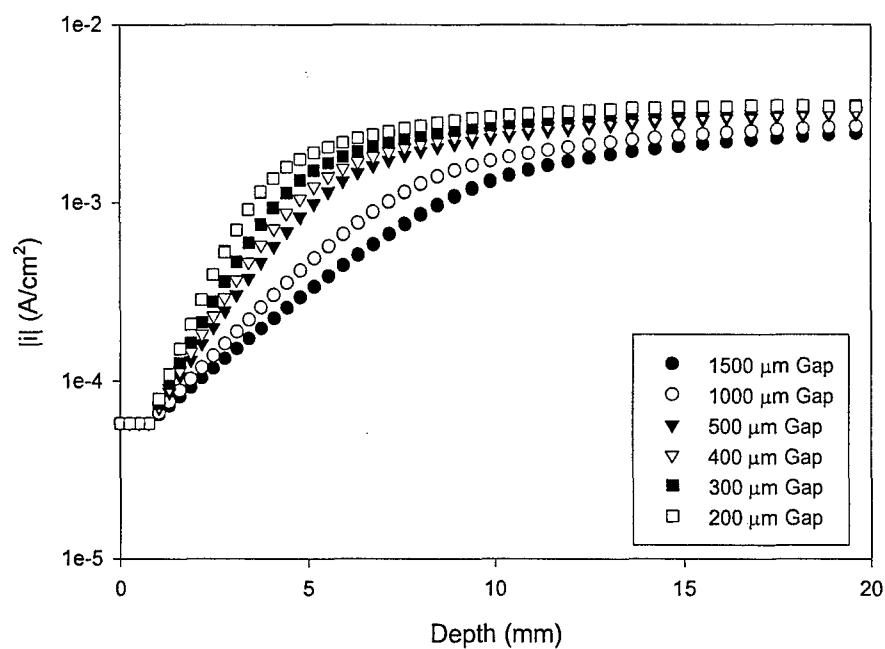
Figure 12. Current density versus depth modeling data for square prism shaped crevice showing (a) i_{anodic} and (b) the absolute value of $i_{cathodic}$. The externally applied potential, E_{app}, was -0.475 $V_{Hg/Hg2SO4}$.

Figure 13. Current density versus depth modeling data for square prism shaped crevice showing (a) i_{anodic} and (b) the absolute value of $i_{cathodic}$. The externally applied potential, E_{app}, was -0.475 $V_{Hg/Hg2SO4}$.

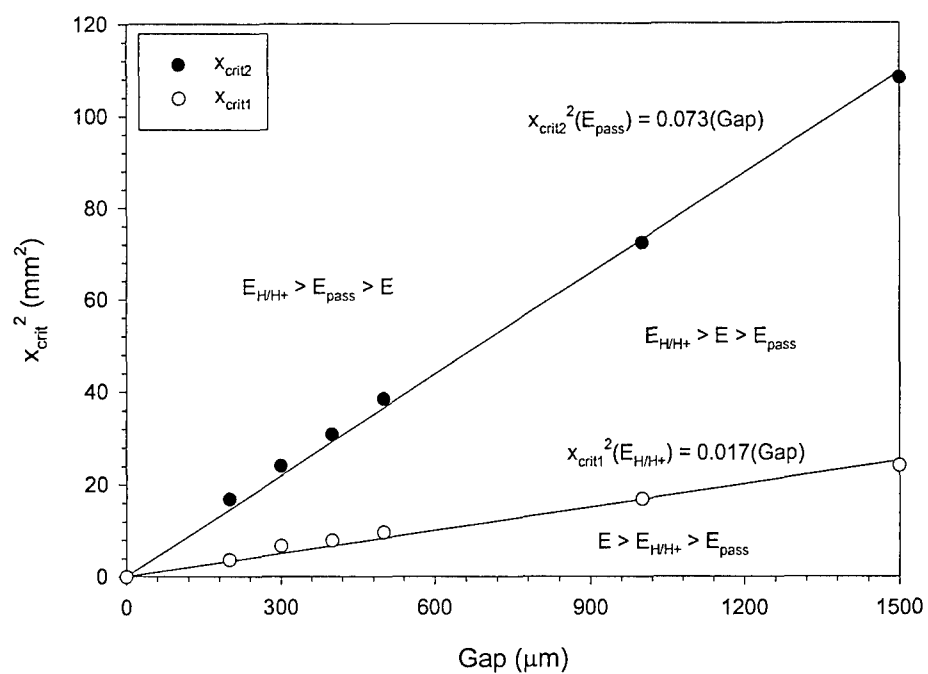**Figure 14.** x_{crit2} versus gap data for PH 13-8 Mo. Two x_{crit} parameters are plotted for conditions: $i_{crit} = 10^{-2}$ A/cm^2, $E_{H/H+} = -0.59$ V Hg/Hg$_2$SO$_4$, $E_{pass} = -0.70$ V Hg/Hg$_2$SO$_4$, $E_{app} = -0.475$ V Hg/Hg$_2$SO$_4$.
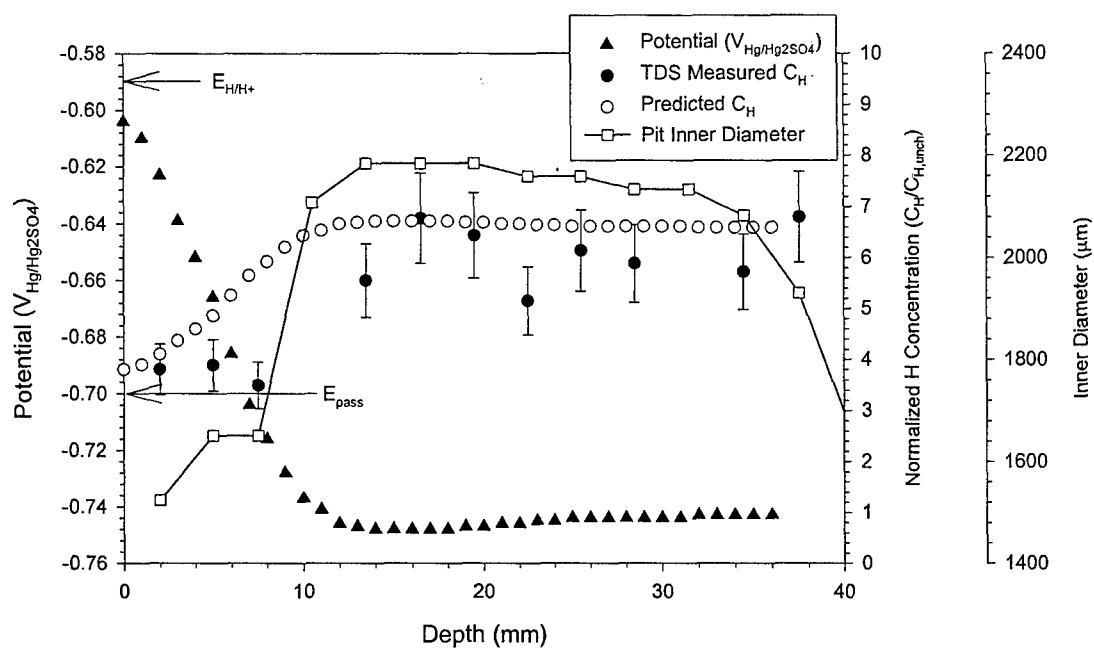
Figure 15. Potential, C_H and pit diameter versus pit depth from a rescaled experimental pit for a 1500 μm diameter by 40 mm depth cylinder exposed to 5 M H_2SO_4 + dissolved metal ions. E_{app} = -0.60 V Hg/Hg_2SO_4
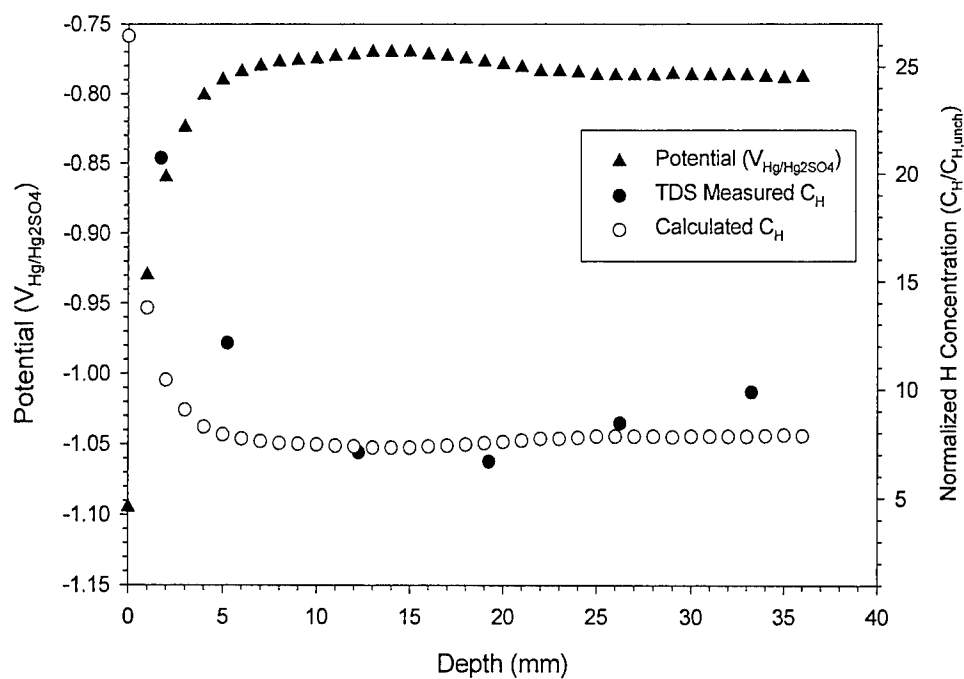
Figure 16. Model pit results for a 1500 um gap and 40 mm depth drilled cylinder in the upright position exposed to 5 M sulfuric acid plus dissolved metal ions. E_{app} = -1.2 $V_{Hg/Hg2SO4}$. $E_{H/H+}$ = -0.59 $V_{Hg/Hg2SO4}$. E_{pass} = -0.70 $V_{Hg/Hg2SO4}$. a) Measured potential, TDS measured C_H, and calculated C_H versus depth.
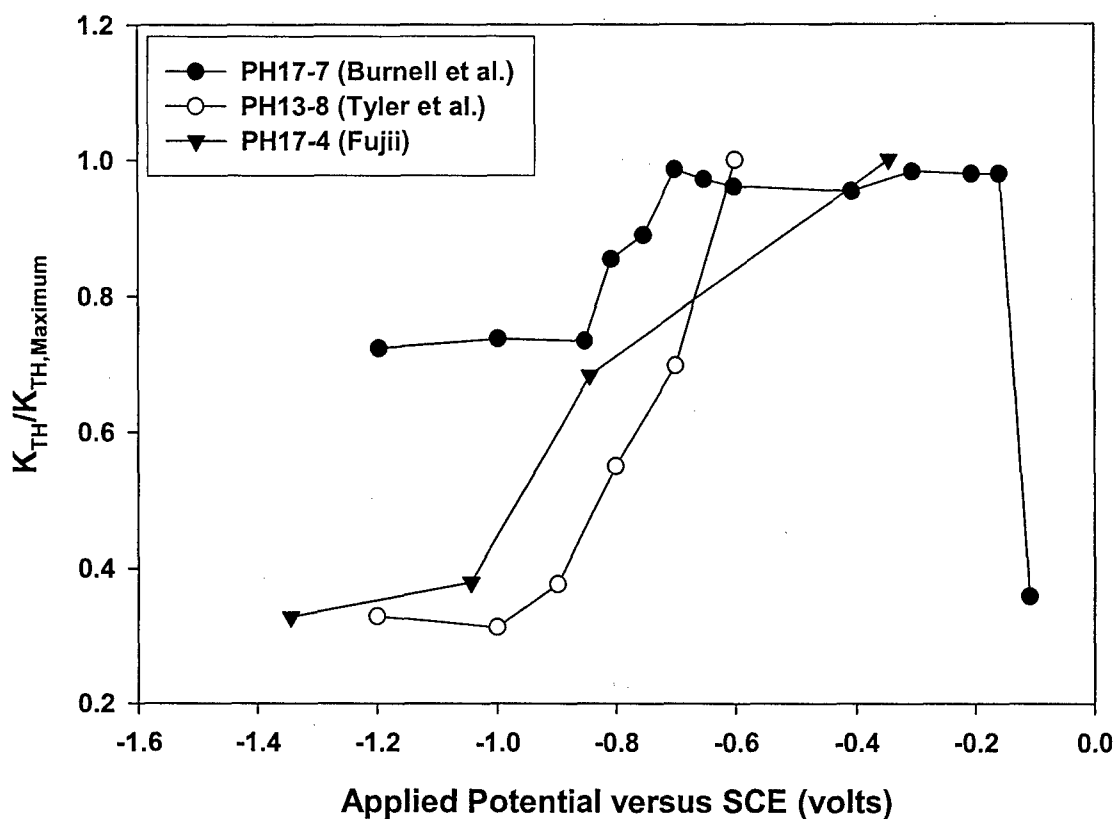
Figure 17. Normalized threshold stress intensity for hydrogen environment assisted crack initiation of pre-cracked precipitation age hardened martensitic stainless steels as a function of applied potential in 0.6 M NaCl solution. Data shown is for high strength (σ_{ys} = 1476 MPa) PH 13-8 (Fe-13Cr-8Ni-2Mo-1Al) [ref. 22], high strength (σ_{ys} =1220 MPa) PH 17-4 [ref. 17], and high strength (σ_{ys} = 1130 MPa) PH 17-7 (Fe-6%Ni-19%Cr-1%Al-03.%Cu)) [ref. 40].

7. REFERENCES

1. R.N. Parkins, *Materials Science and Engineering*, A103, p. 143, (1988).
2. G. Cragnolino, L.F. Lin, and Z. Szklarska-Smialowska, *Corrosion*, 37, 6, p. 312, (1981).
3. Y. Kondo, M. Bodai, M. Takei, Y. Sugita, and H. Inagaki, "Environmentally Assisted Cracking of 3.5NiCrMoV Low Alloy Steel Under Cyclic Straining," Effects of the Environment on the Initiation of Crack Growth: *ASTM STP 1298*, Philadelphia: ASTM, (1997).
4. C.F. Baes, Jr., R.E. Mesmer, The Hydrolysis of Metal Cations, Robert Krieger Publishing Co., Malabar FL, (1986).
5. H.W. Pickering, C. Wagner, *J. Electrochem. Soc.*, 114(7), pp. 698-706, (1967)
6. C.E. Birchenall, *J. Electrochem. Soc.*, 103, p. 618 (1956).
7. K. Muthukrishnan, K.R. Hebert, T. Makino, *J. Electrochem. Soc.*, 151(6), B340-B346 (2004).
8. G.A. Young, Jr., J.R. Scully, "The Effects of Test Temperature, Temper and Alloyed Copper on Hydrogen Controlled Crack Growth of an Al-Zn-Mg-(Cu) Alloy," *H-CDI Conference Proceedings*, Ed. N. Moody, A.W. Thompson, TMS, (2002).
9. B.P. Somerday, L.M. Youing, R.P. Gangloff, Fatigue and Fracture of Engr. Matl Struc., 23, pp. 39-58 (2000).
10. B.F. Brown, In "Stress Corrosion Cracking and Hydrogen Embrittlement of Iron Base Alloys, " Eds., J. Hockmann, J.E. Slater, R. W. Staehle, NACE-5, Houston, TX, pp. 747-750, (1977).
11. K. R. Cooper, R. G. Kelly, J. Chromtag. A 850, pp. 381-9, (1999).
12. H. Okada, In Stress Corrosion Cracking and Hydrogen Embrittlement of Iron Base Alloys, Eds., J. Hockmann J.E. Slater and R. W. Staehle, NACE-5, Houston, TX, pp. 747-750, (1977).
13. E.A. Taqi and R. A. Cottis. In Corrosion Chemistry Within Pits, Crevices and Cracks, National Physical Laboratory; Teddington, Middlesex; UK; 1-3 Oct. 1984. pp. 483-494 (1987).
14. A.M. Brass, J. Chene, A. Boutry-Forveille, Corrosion Sci., 38(4), pp. 569-585 (1996).
15. L.J. Qiao, J. L. Luo, X. Mao, Corrosion, 54(2), p115-120 (1998).
16. K.N. Akhurst and T.J. Baker, Metal and Matl. Trans A, 12A, pp. 1059-1070, (1981).
17. C.T. Fujii, In Stress Corrosion Cracking - New Approaches, ASTM STP 610, ASTM, Philadelphia, PA, pp. 213-225, (1976).
18. L.M. Young, M.R. Eggleston, H.D. Solomon, L.R. Kaisand, Mater. Sci. and Eng. J., A203, p. 377, (1995).
19. W.R. Cieslak, R.E. Semarge, F.S. Bovard, In Microbeam Analysis, editors: A.D. Romig, W.F. Chambers, pp. 303-306, (1986).
20. H.W. Pickering, In NACE 2001 Topical Research Symposium, CORROSION 2001, eds. G.S. Frankel, J.R. Scully, NACE, Houston, TX, (2001).
21. J.R. Scully, J.A. Van Den Avyle, M.J. Cieslak, A.D. Romig, Jr., C.R. Hills, Metall. and Mater. Trans. A, 22A, pp. 2429-2444, (1991).
22. P.S. Tyler, M. Levy, L. Raymond, Corrosion, 47, p. 82, (1991).
23. J.S. Lee, M.L. Reed, R.G. Kelly, J. Electrochem. Soc., 151(7), B423-B433 (2004).
24. S.W. Smith, Ph.D. Dissertation, The University of Virginia, (1995) and S.W. Smith, J.R. Scully, Metall. and Mat. Transactions A, 31A, pp. 179-193, (2000).

25. D. Li, R.P. Gangloff, J.R. Scully, Metall. and Mater. Trans. A, 22A, pp. 2429-2444, (2004).
26. R.G. Kelly, In NACE 2001 Topical Research Symposium, CORROSION 2001, eds. G.S. Frankel, J.R. Scully, NACE, Houston, TX, (2001).
27. Y. Xu and H.W. Pickering, J. Electrochem. Soc, 140, p. 658, (1993).
28. B.G. Ateya, H.W. Pickering, J. Electrochem. Soc., 122, p. 1025, (1975).
29. L.C. Feldman, J.W. Mayer, Fundamentals of Surface and Thin Film Analysis, North Holland, NY, p. 283, (1986).
30. Subramanyan, P.K., Comprehensive Treatise of Electrochemistry, Plenum Press, New York, 1981.
31. N.R. Quick, H.H. Johnson, Acta Met., 26 pp. 903-907, (1978).
32. Interrante, C.G., "Basic Aspects of the Problems of Hydrogen in Steels," *Current Solutions to Hydrogen Problems in Steels*, editors: C.G. Interrante and G.M. Pressouyre, ASM, Ohio, (1982).
33. C.R. Clayton, I. Olefjord, Passivity of Austenitic Stainless Steels, in Corrosion Mechanisms in Theory and Practice, ed. By P. Marcus, J. Oudar, pp. 175-199, (1995).
34. B.G. Ateya, G.Geh, A.H. Carim, H.W. Pickering, J. Electrochem. Soc., 149, pp. B27-33, (2002).
35. N. Lewis, S.A. Attanasio, D.S. Morton, G.A. Young, in "Chemistry and Electrochemistry of Corrosion and Stress Corrosion Cracking," Ed. R.H. Jones, TMS, pp. 421-445, (2001).
36. G.A. Young, Jr., J.R. Scully, "The Effects of Test Temperature, Temper and Alloyed Copper on Hydrogen Controlled Crack Growth of an Al-Zn-Mg-(Cu) Alloy," Metall. and Materials. Trans,
37. C.E. Buckley, H.K. Birnbaum, J. of Alloys and Compounds, 330-332, pp. 649-653 (2002).
38. C.E. Buckley, H.K. Birnbaum, J.S. Lin, S. Spooner, D. Bellmannn, P. Staron, T.J. Udovic, E. Hollar, J. of Applied Crystallography, 34, pp. 119-129, (2001).
39. C.S. Carter, D.G. Farwick, A.M. Ross, J.M. Uchida, Corros. J., 27, p.190, (1971).
40. G. Burnell, D. Hardie, R.N. Parkins, Br. Corros. J., p.229, Nov. (1987).
41. K. Cho, M.I. Abdulsalam, H.W. Pickering, J. Electrochem. Soc., 145, p. 1862, (1998).
42 J.N. Al-Khamis, H.W. Pickering, J. Electrochem. Soc., 148, pp. B314, (2001).
43. C.F. Barth, E.A. Steigerwald, and A.R. Troiano, Corrosion, 25, p. 353-358, (1969).
44. R.J. Gest, A.R. Troiano, Corrosion, 30, p. 274-279, (1974).
45. A. Sehgal, B.G. Ateya, H.W. Pickering, Acta Mater. 45, p. 3389 (1997).